SOFT ROBOTS

Desktop fabrication of monolithic soft robotic devices with embedded fluidic control circuits

Yichen Zhai[1]*, Albert De Boer[2], Jiayao Yan[1], Benjamin Shih[1], Martin Faber[2], Joshua Speros[3], Rohini Gupta[3], Michael T. Tolley[1]*

Most soft robots are pneumatically actuated and fabricated by molding and assembling processes that typically require many manual operations and limit complexity. Furthermore, complex control components (for example, electronic pumps and microcontrollers) must be added to achieve even simple functions. Desktop fused filament fabrication (FFF) three-dimensional printing provides an accessible alternative with less manual work and the capability of generating more complex structures. However, because of material and process limitations, FFF-printed soft robots often have a high effective stiffness and contain a large number of leaks, limiting their applications. We present an approach for the design and fabrication of soft, airtight pneumatic robotic devices using FFF to simultaneously print actuators with embedded fluidic control components. We demonstrated this approach by printing actuators an order of magnitude softer than those previously fabricated using FFF and capable of bending to form a complete circle. Similarly, we printed pneumatic valves that control a high-pressure airflow with low control pressure. Combining the actuators and valves, we demonstrated a monolithically printed electronics-free autonomous gripper. When connected to a constant supply of air pressure, the gripper autonomously detected and gripped an object and released the object when it detected a force due to the weight of the object acting perpendicular to the gripper. The entire fabrication process of the gripper required no posttreatment, postassembly, or repair of manufacturing defects, making this approach highly repeatable and accessible. Our proposed approach represents a step toward complex, customized robotic systems and components created at distributed fabricating facilities.

INTRODUCTION

In recent years, soft robots have provided an attractive approach to solving complex tasks simply and inexpensively, like interacting safely with humans and fragile objects (1–3). To date, the most popular method for the fabrication of soft robots has been cast molding with two-part silicones. This fabrication approach has achieved components with low stiffness using simple equipment to make robots capable of locomotion (4–9), manipulation (10–16), swimming (17–19), haptic display (20), rehabilitation (21, 22), and pumping liquids (23). Recent work has also embedded soft robots with electronics-free pneumatic control circuits to achieve complex autonomous soft robots with promising interactive sensing and feedback functions or self-sustained rhythmic motions (9, 15, 16, 24, 25). However, previous soft robots have been mainly fabricated in multiple steps using silicone molding processes followed by manual assembly of subsystems. Some previous soft robots consist of three-dimensional (3D)–printed or mechanically processed components, whereas the direct 3D printing of fully functional robots has long been a goal (26–32). Until now, the final assembly has always been required. The manual fabrication and assembly steps required to manufacture soft robots place upper limits on the complexity and repeatability of existing soft robots and require considerable engineering knowledge and experience to fabricate.

Recently, emerging 3D printing technologies have shown potential advantages for the monolithic fabrication of complex soft robots with high repeatability and low manual labor requirements (33, 34). The printing approaches include inkjet printing, stereolithography (SLA), and fused filament fabrication (FFF; also known as fused deposition modeling or FDM). Comparing the features of these various fabrication approaches (including silicone molding) and the associated typical material properties (fig. S1), the main advantages of the traditional silicone process are the high softness and the low cost of material, whereas the required manual labor for molding is the highest among all approaches. Inkjet printing is most commonly accomplished with Stratasys Connex printers, which are able to deposit multiple materials in monolithic printing workflows for complex composite structures (21, 31, 35–39). However, the high cost of the equipment and materials and health hazards associated with chemicals involved in the processes (40–42) limit the accessibility of this fabrication approach. Also, the high viscosity and damping of the soft materials available for inkjet printing limit their applications in soft robotics (for example, viscous materials respond slowly to applied pressures or stresses).

SLA printing uses digital light patterning, which can generate complex structures with high resolution (43–45). However, disadvantages of SLA printing include the toxicity of the raw liquid resin (40–42) and the low elongation strength [100% for soft SLA resin versus 650% for thermoplastic polyurethane (TPU) used in FFF; fig. S1] (46–48) of the printed parts. In addition, this approach requires support structures, and supporting materials cannot be removed from hollow cavities. As a potential solution, controlling the inclined angles of overhanging features or inclining whole 3D designs in the slicing process may allow for printing without inner support using SLA printers. However, this approach often

[1]Department of Mechanical and Aerospace Engineering, University of California, San Diego, La Jolla, CA 92093, USA. [2]BASF 3D Printing Solutions B.V., Emmen, Netherlands. [3]BASF Corporation California Research Alliance, Berkeley, CA 94720, USA. *Corresponding author. Email: yiz659@eng.ucsd.edu (Y.Z.); tolley@ucsd.edu (M.T.T.)

requires extra design work and many bottom tree supports that require additional postprocessing to remove.

In contrast with other fabrication methods, FFF is the most affordable, uses nontoxic materials, and can thus be more easily adopted by nonspecialized users at different facilities. FFF printing, in combination with the design approach that we describe in this work, requires the least manual labor among the fabrication approaches, and the available TPU materials have high strength and low viscosity, making them suitable for soft robots. The main challenge is that the material has relatively high stiffness, which makes the printed soft robotic devices less competitive in output performance compared with the products from other approaches. In addition, FFF uses a modeling process that composes a 3D structure from individually printed traces in an inconsistent way. The difference in the time required to deposit material between parts and the free motion of the printhead between discontinuous segments can cause undesired flaws and pinholes, which lead to severe air leakage in soft pneumatic devices. Previous research has mainly focused on increasing the thickness of the shells in the designs to minimize air leakage; however, this has resulted in structures with very high stiffness. As a result, FFF has mainly been used to fabricate simple devices, such as bending actuators (43, 49–59), because the inconsistent modeling/printing process has prevented the printing of functional complex structures (such as those required for sensing and logical control). Thus, we found the low softness of TPU material and the high risk of air leakage from the printed structures to be the main challenges in 3D printing soft pneumatic robots using FFF.

Previous work has frequently demonstrated the performance of printed devices by the output force of soft actuators (49–51); however, we believe that the most important performance metric is the thinnest achievable airtight walls. The reason is that the output force of actuators results from the pressure of the air applied in the actuator. As long as the device does not burst, high forces can be achieved with high pressure acting over large areas. When the devices are actuated, the stress of the structures themselves adds more resistance, which prevents the actuators from reaching higher actuation strain and stress. Therefore, the actual performance of soft pneumatic devices should be related to the structural softness, and, in the printing approach, it is shown as the thinnest achievable airtight walls.

In this work, we present a design method of 3D printing monolithic airtight, high-performance, and complex soft pneumatic robots using a commercially available desktop FFF printer. The first key design rule for obtaining airtight structures is to print them using a single, continuous toolpath for each soft pneumatic device, known as an Eulerian path (60). A second key design rule is to create structures with very thin walls (about two traces thick), resulting in structures with low stiffness comparable to silicone-molded parts (yet still airtight if the first rule is followed).

Following these rules, we were able to manufacture thin walls that experience low internal stress for a high range of actuation pressures. As a result, we were able to fabricate bending actuators, control valves, and other airtight structures, each from a single continuous toolpath. Furthermore, we demonstrated that these individual devices can be combined to form complex robotic systems with their toolpaths merged into a single Eulerian path. Because all the individual components followed the appropriate design rules, the combined system could be monolithically printed in a one-shot workflow while maintaining the airtightness and soft actuation performance of each component.

Following our design method, customized electronics-free pneumatically driven soft robots could be fabricated with the desired functions. We demonstrated this method using the example of an autonomous gripper (Fig. 1).

RESULTS

Toolpath design for airtight pneumatic devices

Traditional molding and casting processes fabricate homogenous 3D parts. In contrast, FFF printing can lead to inconsistently connected pieces because they are accumulations of printing toolpath traces, which are not generated simultaneously. This process can result in many defects that allow air to leak from printed pneumatic devices caused by pinholes, gaps, and issues with merging adjacent traces. Also, because of the high elasticity of soft TPU filament, the control of the flow rate of material through the printing extruder is less precise compared with that of the rigid filaments, which increases the risk of defects in the results. In most of the previous works, the solution for this issue has been either to increase the thickness of the walls of the pneumatic devices or to use a very low printing speed (<10 mm/s) (43, 49, 51, 61). However, because
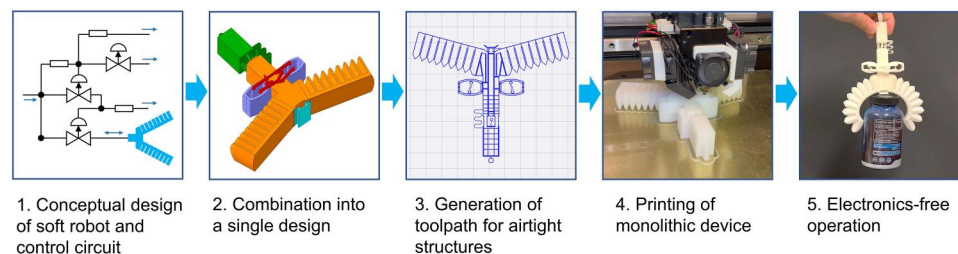
Fig. 1. Workflow for desktop digital fabrication of autonomous monolithic soft robotic devices with embedded fluidic control circuits. (1) On the basis of the expected functions, control and actuation units were combined in a logical control circuit as a conceptual design. (2) We designed the robotic device with an integrated control circuit by combining multiple individual (previously characterized) components into a single CAD file. The components may include actuators, control valves, sensors, tubing, and frame structures. (3) The printing toolpath is automatically generated by slicing software with appropriate parameters, which enforces the design requirements of being airtight and achieving the desired performance. (4) We then used the toolpath file to print the monolithic robotic device. The process required no manual assembly or posttreatment, which minimized the skill required for manufacturing and enabled duplication with high repeatability. (5) Right after printing, the device was ready for electronics-free operation when connected to a supply of pressurized gas. During operation, the embedded fluidic control components provided capabilities such as autonomous sensing or feedback control without an electronic microcontroller.

1. Conceptual design of soft robot and control circuit
2. Combination into a single design
3. Generation of toolpath for airtight structures
4. Printing of monolithic device
5. Electronics-free operation

TPU is stiffer than the soft materials used in other fabrication methods, a thicker wall would result in printed parts with a higher structural stiffness, making them less suitable for soft robotics. Also, a low printing speed would result in a long printing time, limiting the efficiency of fabrication with large-scale and complex designs.

To 3D-print airtight pneumatic structures, we were able to address most of the issues with air permeability by tuning the control parameters in the slicing software (for example, by increasing the extrusion temperature, decreasing the layer height, and increasing the overlap between traces). These settings helped to remelt the surface portion of the previously printed part for better bonding with the newly extruded trace. The extrusion temperature was set to 230°C (slightly lower than the thermal decomposition temperature of the TPU material). A low layer height (0.1 mm) enabled the conduction of heat between the layers and improved bonding with previously printed layers. For the adjacent traces on the same layer, we found that a 0.1-mm horizontal overlap caused the two traces printed through a 0.4-mm nozzle to merge and form a tight structure. Thus, we used this horizontal overlap in all of our designs. Using these printer settings, we were able to reduce the air permeability of our printed parts such that vertical walls with a thickness of only two traces were nearly airtight.

However, using the optimized printer settings discussed above, there were still a number of small leaks left in the printed structures, which were the result of discontinuous extrusion toolpath segments connected by free motion (to be specific, motion with no extrusion; Fig. 2A). To understand this, consider a design with two hollow cylinders that are required to be airtight [the CAD (computer-aided design) design depicted in Fig. 2A]. Because the two cylinders are separated, in the toolpath (the lower left drawing in Fig. 2A), the printing nozzle needs to perform a sequential operation of filament retraction, free motion, and the resumption of filament extrusion to build a connected path. Material retraction is a feature of FFF printing to prevent material from leaking through the nozzle during free movement of the nozzle between separated segments. However, when printing with soft filaments, we noticed that this retraction was ineffective because the stretchability of the filament caused the material to extrude (drip) during the free motion of the printhead. At the retraction point, the nozzle removed some material from the structure, which often caused a pinhole (see Fig. 2A). Meanwhile, at the point where a new path started, the lack of material often caused another pinhole. The strings caused by the dripping material can be seen in the upper right photograph in Fig. 2A, and the presence of pinhole defects can be seen in the micrographs.

We found that an effective method to avoid defects caused during material retraction and restarting printing was to completely avoid the use of retraction and free movement on the vertical walls of a print. On the basis of this concept, we devised a corresponding approach, which we call "Eulerian path printing," in which the printing nozzle is traced through the whole pattern in a single continuous path without interruption. Because the generation of a toolpath involved a lot of work and was usually performed by slicing software, we defined three design rules for the original CAD design that caused the automatic slicer to generate Eulerian paths. First, all the vertical walls were required to have a width exactly twice the width of a single printed trace. Second, all the components were required to be interconnected on all layers without any independent island structures. Last, we required no closed loop structures in the

parts (for example, the cylinder loops in Fig. 2A). Note that, for the first rule, more generally, the wall widths could be any positive even integer multiple of the width of a single trace to form Eulerian paths, as long as all the walls shared the same width. We set this number to two to achieve thin and soft structures.

As an example of applying these rules to generate an Eulerian path design, two independent cylinders can be connected by an extra pathway to generate a continuous path (Fig. 2B, upper left). If the relative mechanical movement was required between the two cylinders, then the connecting pathway could be designed with a serpentine shape or could be broken up into disconnected free-hanging structures (fig. S4) to reduce its effective stiffness. On each of the two cylinders, a thin gap with a width of 0.03 mm has been applied to cut the loops and force the slicer to generate an Eulerian path. The actual toolpath of this structure is shown in the lower left drawing of Fig. 2B. The whole pattern was completed in a single continuous path. The print settings were selected such that there was an overlap between the traces (to be specific, the slicer planned toolpaths for printing traces with an offset distance smaller than the diameter of the nozzle); the thin gaps mentioned above were merged in the printed outcome (Fig. 2B).

Using the aforementioned rules to generate Eulerian toolpaths, we designed a bending pneu-net style fluidic elastomer actuator (Fig. 2C) (7, 62). The actuator consisted of multiple hollow blocks. When the blocks were inflated, the walls between two adjacent blocks pressed on one another, causing the whole actuator to bend. To prevent the vertical planes of the actuator from bulging, we added inner supporting walls between the backplane and the front blocks (Fig. 2C). When the supporting walls were added, small local loops formed in every block unit would break the Eulerian path into multiple separated paths. Therefore, a thin gap was added to the design on each of the supporting walls.

To demonstrate the airtight performance of actuators printed in the Eulerian path, we fabricated three actuators with different designs and printing control strategies. We used commercially available software (ideaMaker, Raise3D) to automatically generate the toolpaths for 3D printing the parts. We then tested the airtightness of each part by inflating it when submerged in water (Fig. 2, D to F). The first actuator (Fig. 2D) was designed without an Eulerian toolpath, and the slicing control parameters were also based on common settings more suited for rigid filaments. The printed actuator was inflated by a pressure of 14 kPa. The test showed many large leaks, which were distributed on both the vertical walls and the horizontal planes at the top and bottom of the actuator. The leaks on the vertical walls were due to the delamination of the printed traces on many layers. We hypothesized that this delamination was caused by an inconsistent wall thickness in the design and poor contact between the traces of the walls. For the horizontal walls, even when the filling density was set to 100% in the slicing software, the actual volume of extruded materials was still often less than the volume of the wall structure in the design. We concluded that this shortage of infill resulted in mesh holes between the traces, which account for the large leaks through the horizontal planes.

In the second actuator design, we unified the wall thickness to a constant valve and applied a forced overlap between the traces to ensure proper contact between the traces and generate an airtight part (Fig. 2E). Because the slicing software did not have the option to apply an overlap between traces in the horizontal direction, we achieved one by setting the nozzle diameter to 0.3 mm in
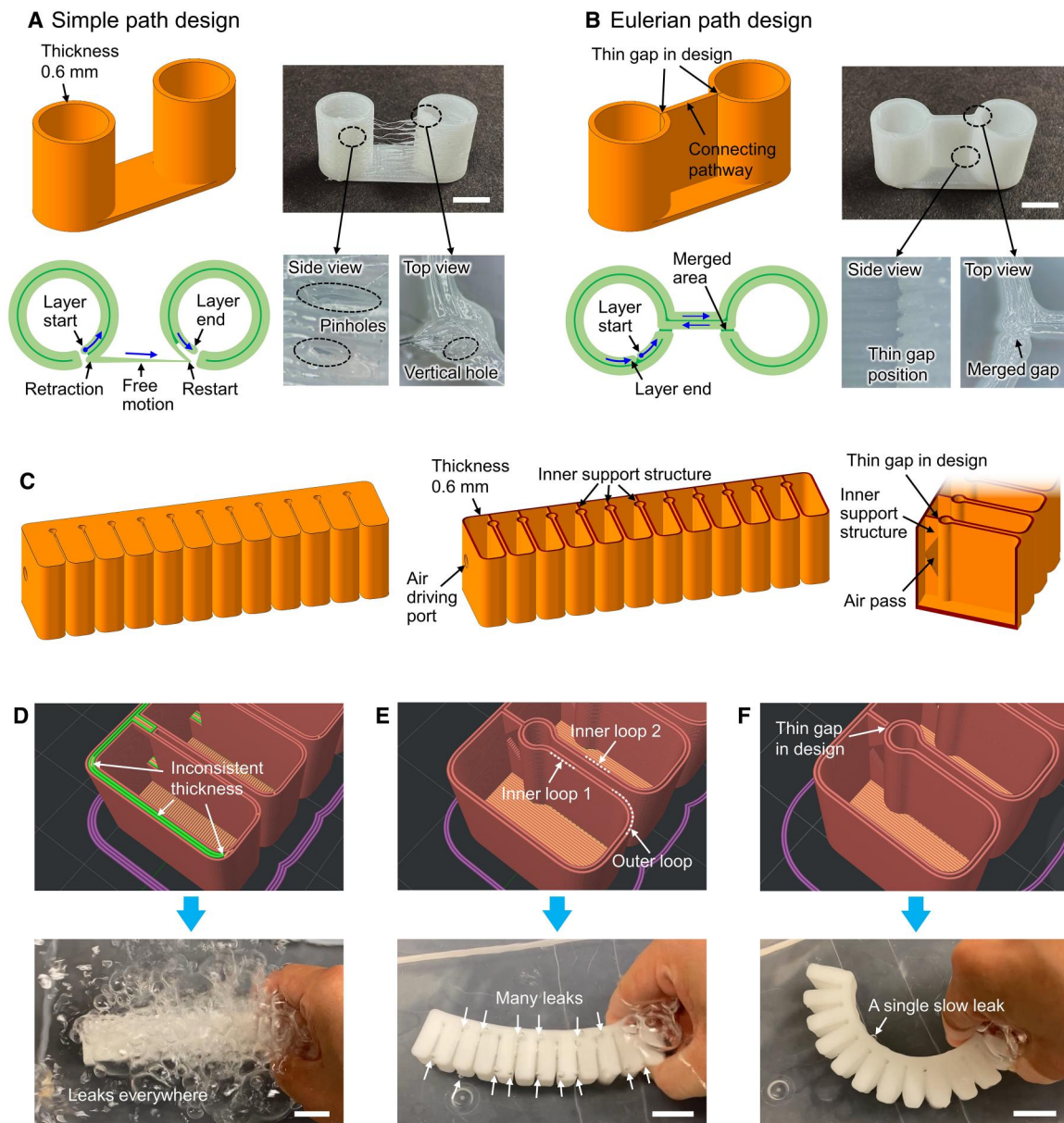
Fig. 2. Design rules for airtight structures. (**A** and **B**) Comparison of the air permeability of printed pneumatic actuators designed using (A) a naive approach and (B) an approach that leads to Eulerian toolpaths. In each panel, the upper left image is the CAD design; the lower left image is the printing toolpath of one layer; the upper right photographs demonstrate the actual printed parts, and the lower right optical micrographs show the presence/absence of defects. The scale bars on the photographs represent 5 mm. (**C**) CAD design of a bending actuator (left) with horizontal (middle) and vertical (right) section views. (**D** to **F**) Comparison of a bending actuator with three different toolpath designs. The upper images are the generated toolpaths, and the lower photographs show the leakage tests by inflating the printed parts underwater (movie S1). The scale bars on the lower photographs represent 2 cm. (D) A simple design with inconsistent vertical wall thickness led to many leaks. (E) An improved design with unified wall thickness and denser infill had a small number of leaks. (F) A design that used only Eulerian toolpaths had only one leak.

the software, whereas we physically used a 0.4-mm-diameter nozzle for printing. Meanwhile, the wall thickness in the CAD design was unified to 0.6 mm to ensure a wall thickness of two traces on all vertical walls. On horizontal planes, we used the same overlap strategy to generate dense infill to avoid the formation of a leaky mesh. The printing parameter settings are summarized in table S1. As a result of these improvements in printing settings, the test with an inflating pressure of 14 kPa showed only finite leaks (Fig. 2E, bottom).

The remaining leaks were at the retraction and restart points on each block unit. To avoid the retractions associated with these local loops in the toolpath, we cut the CAD design to connect all the segments into a single Eulerian path. In the design shown in Fig. 2C, we added thin gaps in the inner support walls (which did not appear in the printed part because of the overlap between the traces). The corresponding Eulerian toolpath is shown in Fig. 2F. The printing of this actuator took 6 hours and 2 min. When printed with this toolpath, there was only a single random leak on the device with an

inflating pressure of 34 kPa, which was not large enough to prevent its successful operation (Fig. 2F). Videos of the underwater tests are attached as movie S1.

In general, we found that, because of defects in the filament, fluctuations in the nozzle temperature, or material stuck to the nozzle, random pinholes occurred when printing a single trace of TPU. When using an Eulerian toolpath with two traces, most of the pinholes in a single trace were filled by an adjacent trace. The occasional pinholes that remained in the final parts printed in this manner were too small to have a large influence on the successful pneumatic actuation of the corresponding soft robot components.

To further demonstrate the airtightness of devices printed in the Eulerian path, we printed two grippers composed of bending actuators printed with non-Eulerian and Eulerian toolpaths (to be specific, composed of the actuators shown in Fig. 2, E and F, respectively). The printing control parameters for the two grippers were all identical, whereas one used a non-Eulerian path design, and the second used an Eulerian path design (see movie S2). Each gripper was pressurized to an initial pressure of 23 kPa by injecting a fixed volume of air (about 35 ml) from a syringe to grip and hold a tennis ball. We then counted the holding time (the time until the tennis ball was released because of air leakage through the gripper). The non-Eulerian gripper held the ball for 4 s, whereas the Eulerian gripper held it for 96 s.

On the basis of these results, the high-level manufacturing approach for printing thin airtight pneumatic devices from TPU filaments using FFF can be summarized with two items. First, we applied a horizontal overlap of 25% between each printed trace. Second, we used an Eulerian path on each layer of the print containing vertical walls. Note that we did not find it necessary to apply an Eulerian path to the bottom and top horizontal layers of the device because we found a dense infill to be sufficient for the airtight sealing of these layers. The design and printing control parameters are in table S1, which were tuned on the basis of our printing setup (E2 printer, Raise3D) equipped with a 0.4-mm brass nozzle.

Designing bending actuators with high structural softness

Because commercially available TPU material for FFF printing is relatively rigid (Shore 80A) compared with other materials used to fabricate pneumatic soft robots (fig. S1), the printed pneumatic devices with similar geometries show lower performance when printed from TPU. For example, a TPU actuator would have much lower displacement and output force when actuated as compared with a silicone actuator with the same geometry and actuation pressure, because a large portion of pressure is used to overcome the stress of the TPU structure itself. This motivated us to find ways to increase the structural softness of our devices. We found this approach preferable to looking for softer filaments because we found filaments with Shore hardness lower than 80A to be difficult to extrude on multiple common desktop printers (Raise 3D N1, N2, and E2; Flashforge Guider; and Prusa i3), resulting in low print yields.

We designed our first airtight actuator to have rectilinear actuation units (Fig. 3A). When the actuator was pressurized, the bending deformation was realized by inflating the vertical walls between the units so that the bending actuation range was related to the displacement of each vertical wall when inflated. In analyzing the performance of the initial design, we noticed that the actuation of the vertical walls was constrained by the thick planes at the top and bottom of the actuator and the enhanced stiffness due to the rectilinear corners. The planes also made the actuator stiff in compression (limiting performance in antagonistic configurations). We improved the actuator design by modifying the shape of the actuation walls from plane to curved cylindrical and spherical shapes, so the top and bottom planes were greatly reduced, and the rectilinear edges were replaced by rounded edges (Fig. 3B). Inside the actuator, there were still inner supporting walls to hold the backplane on the front units (Fig. 3C), and the vertical walls had a thickness of 0.6 mm. The printing of the curved actuator took 4 hours and 38 min.

We compared the structural softness of the two different designs (Fig. 3D). The curved actuator had a lower bending stiffness in both forward and backward directions as compared with the rectilinear actuator. When actuated, the curved design was able to form a complete circle with modest positive pressure (24.1 kPa, or 3.5 psi) and also bent in the opposite direction with negative applied pressure (Fig. 3E). Thus, the actuator had one or two orders of magnitude higher structural softness than all FFF-printed TPU bending actuators that have been described previously in the literature. Most previous actuators could not form a whole circle even at the highest tested pressure (table S2) (43, 49–52, 58, 61). Because the curved units were compressible, the actuator also showed a large backward bending strain when a negative pressure was applied (Fig. 3E). For a detailed characterization of the actuator, please see fig. S2.

With two curve actuators, we assembled a soft gripper, as shown in Fig. 3F. At 103.4-kPa (15.0 psi) supplied pressure, the gripper could robustly hold an open-top water container with a total weight of 1.3 kg (movie S3). To grip an object, we first supplied −13.8 kPa (−2 psi) to open the two actuators of the gripper, then we applied 103.4 kPa (15.0 psi) to firmly grasp the object.

Combining two curved actuators back-to-back into a single CAD design, we demonstrated a bidirectional swing actuator. The printing time of this actuator was 15 hours and 49 min. We tested this actuator driven by differential pressures supplied to the two sides, causing the actuator to swing back and forth rapidly (Fig. 3G). A potential application for this actuator includes limbs for mobile soft robots.

Monolithic printed pneumatic valve

Autonomous electronics-free soft pneumatic systems have been demonstrated previously using both soft actuators and control components (9, 15). In these designs, pneumatic valves have been used as control components, consisting of a hollow channel and an actuation chamber. In the open state, the air was able to flow through the inside of the channel, whereas, in the closed state, the pressurized actuation chamber applied force on the channel to shut off the airflow. Because there were multiple hollow structures in the valve, traditional fabrication methods required several steps to prepare for the individual components by printing, molding, or cutting, followed by final assembly and tuning processes (15, 24, 63). These processes required a lot of manual labor and skill to consistently achieve functional devices. Using the approach described here, we designed a pneumatic valve that could be printed monolithically, without any manual posttreatments (for example, assembly, adjustment, or repair).

Similar to previous work, our control valve had three input ports, two of which were connected by a channel, and a third port connected to an actuator that kinked the channel when pressurized (Fig. 4). Two curved walls on the inner side of the valve served as
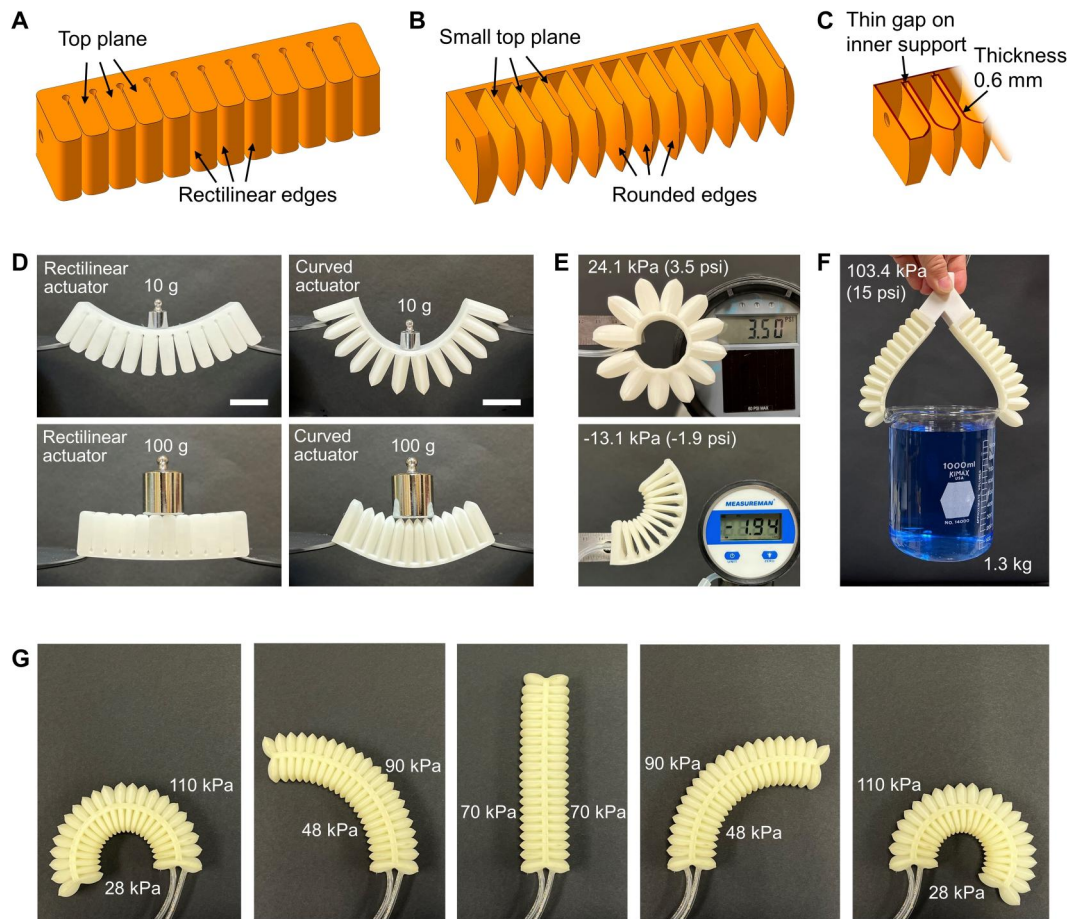
Fig. 3. Design of bending actuators with curved walls instead of rectilinear walls for higher structural softness. (**A**) CAD design of a bending actuator with rectilinear walls. (**B**) CAD design of a bending actuator with curved walls. (**C**) Section view of the curved actuator. (**D**) Comparison of the structural softness between the rectilinear and curved actuators. The upper photographs demonstrate the bending of the two different actuators (with zero gauge pressure internally) in the actuation direction, under a weight of 10 g. The lower photographs demonstrate the bending of two different actuators (with zero gauge pressure internally), in the direction opposite that of actuation, under a weight of 100 g. The scale bars represent 2 cm. (**E**) Curved actuator with positive and negative pressure applied internally. (**F**) Curved actuator lifting a 1.3-kg load at an internal gauge pressure of 103.4 kPa. (**G**) Demonstration of a bidirectional actuator with differential pressures supplied to the left and right chambers.

membranes that displace when pressurized to actuate the valve (to be specific, kink the channel between them). Bends on the edge of the membranes increased their softness and actuation range. Additional pathways between different components connected the entire valve into a single part on all the layers to comply with the Eulerian path design rule.

We actuated the valve to test its functionality (Fig. 4B). In the open state, the chamber was not actuated, so the channel remained in the original printed state, and the air was able to flow through the channel. In the closed state, the inflated chamber applied a compressing force to kink the channel and shut off the airflow (movie S4).

To optimize the control valve, we made use of the analogy to existing electronic components. The pneumatic valve worked similarly to a metal-oxide semiconductor (MOS) transistor, in which the voltage applied on the gate electrode controls the current from the drain to the source. Moreover, similar to transistors, the ratio of the flow through the channel of the pneumatic valve when open versus the leakage when closed (the on/off ratio) was an important

performance metric. Because the closing of the valve fully relied on mechanical deformation of the soft components, we found that the unexpected deformation and rough surface finish inside the channel could cause high leakage. To address this challenge, we investigated two strategies to improve the performance by optimizing the vertical and horizontal cross-sectional shapes of the channel.

We found the shape of the vertical cross section of the 3D-printed channel at the center of the control valve to play a critical role in the performance of the valve. We originally designed the vertical cross section of the channel to have a diamond shape (Fig. 4C). Although we generally used a wall thickness of 0.6 mm in our designs, for this part, we used a wall thickness of 0.32 mm. Because the nozzle was defined to be 0.3 mm in diameter in the slicing software, it still printed two traces on the 0.32-mm vertical wall, with a higher overlap ratio and a lower extrusion rate. Once printed, when the channel with a diamond cross section was kinked, the two walls of the channel were pushed together to seal the opening (similar to a kinked garden hose). However, because
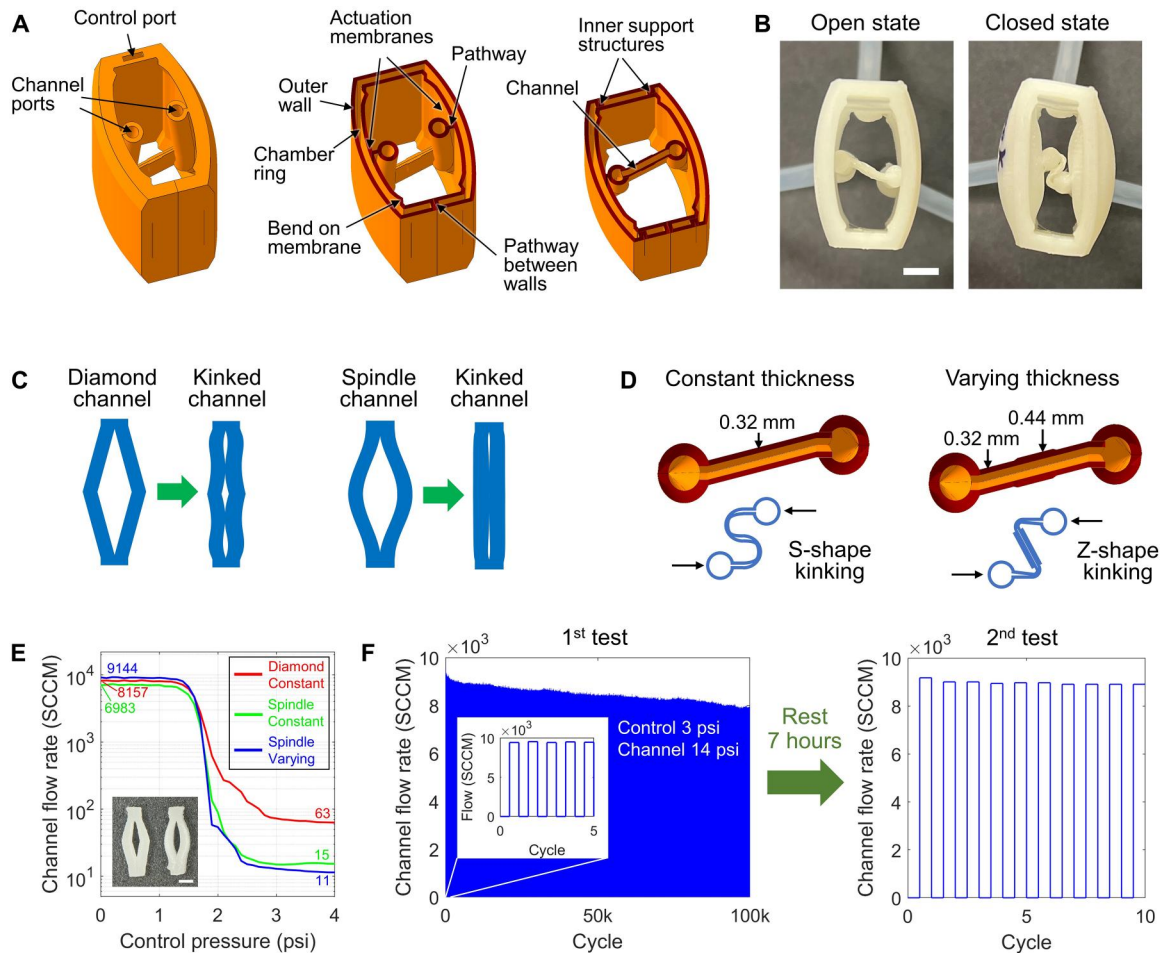
Fig. 4. Design of monolithic printed pneumatic valve. (**A**) CAD design of a printed normally open valve with section views at two different heights showing the inner structures. (**B**) Photographs of the printed valve in the open and closed states. The scale bar represents 5 mm. (**C**) Alternative channel designs with different vertical cross-sectional shapes, along with the hypothesized kinked states. The central white area is the channel opening, and the two sides in blue are the walls. The diamond shape (left) allowed more flow when kinked than the spindle shape (right). (**D**) Horizontal cross-sectional views showing two different designs of the channel wall with anticipated kinked states: constant wall thickness (left) and varying wall thickness (right). (**E**) Flow rate of two valves due to 96.5-kPa (14 psi) constant pressure supplied to the channel. The unit of flow rate is standard cubic centimeters per minute (SCCM). The red curve represents a valve with a diamond channel shape and constant wall thickness. The green curve represents a valve with a spindle channel shape and constant wall thickness. The blue curve represents a valve with a spindle channel shape and varying wall thickness. The inset shows an optical micrograph of the cross sections of the diamond channel (left) and spindle channel (right). The scale bar represents 1 mm. (**F**) Durability test of a valve with 100,000 repeated operation cycles. The inset shows a detailed view of the first five cycles. A second test was performed after the durability test and a rest period of 7 hours (right).

of the stiffness of the material, the two acute angles of the diamond could not deform to 0°, and the two obtuse angles could not deform to 180°, resulting in small openings even in the kinked state (Fig. 4C). As a result, we measured a relatively high rate of airflow through the valve in the closed state (Fig. 4E). To address this leakage of the valve when closed, we modified the cross-sectional shape of the channel to have a spindle shape. As a result, the holes that remained in the kinked state were smaller and allowed a lower amount of air to leak through as compared with the valve with a diamond-shaped channel.

Aside from the vertical cross section, we also tested varying channel shapes when viewed from a horizontal cross section (Fig. 4D). First, we found that a channel that was inclined (rather than perpendicular) to the membranes effectively applied an eccentric load, which reduced the force required to buckle (kink) the

channel (*64*). In addition, we tested the ability of a channel with varying thickness to localize the kinks in the tube and improve the valving (Fig. 4D). We found constant thickness channels to deform into an "S" shape in the kinked state, resulting in a relatively high rate of leakage flow. Taking advantage of the capabilities of 3D printing, we created another design with an increased wall thickness in the middle third of the channel. Because of the higher bending stiffness of the thicker segment, the kinks in the channel were localized to the sections with thinner walls, resulting in a "Z" shape in the kinked state and reduced leakage flow.

We characterized the performance of valves using the different channel designs described above (Fig. 4E). For each valve, we applied a constant input pressure of 96.5 kPa (14.0 psi) to one channel port and measured the flow rate of air at the other channel port corresponding to various pressures supplied to the

control port. In the open state, the valve that improved using both strategies (to be specific, with a spindle cross-sectional shape and varying wall thicknesses) showed a 10% higher flow rate compared with the original one. Meanwhile, in the closed state, the air leakage was reduced by 80%. We empirically defined the closing threshold of the valve as the control pressure that reduced the channel flow to below 50 SCCM (standard cubic centimeters per minute), because such a flow rate did not affect the logic of pneumatic robots in the operation period. With such a definition, the control threshold of the improved valve was 13.8 kPa (2.0 psi), at which it could shut off a channel pressure up to 137.9 kPa (20.0 psi) (movie S4). For detailed characterizations of valves with varying cross-sectional shapes and wall thicknesses, please see fig. S3.

Besides measuring the flow through the valve in the "on" and "off" states, durability is also an important metric for use in robotic systems that may require many operation cycles. To test the durability of the valves, we supplied a 14-psi constant pressure to the channel and periodically pressurized the control port to 20.7 kPa (3.0 psi) to close and open the valve repeatedly for 100,000 cycles with a period of 4 s (Fig. 4F, left). In all the testing cycles, the valve worked functionally in both open and closed states. Because of the long-term viscoelastic deformation of the TPU material, after being kinked many times, the channel did not fully recover to the original cross-sectional opening area, which was shown as a decreasing open-state flow from 9.4×10^3 to 7.9×10^3 SCCM after the testing cycles. After a rest period of 7 hours, the flow in the open channel was recovered to 9.0×10^3 SCCM (Fig. 4F, right).

In summary, we designed a monolithically printed soft pneumatic valve with good performance on three key metrics: first, a high "on/off ratio" or ratio of flow in the "on" state versus flow in the "off" state; second, low leakage in the off state; last, high durability. We designed each valve to be 3D-printed in layers consisting of Eulerian toolpaths, which ensured their airtightness and robustness during operation. The printing time of the valve was 1 hour and 7 min, and the process did not require any manual posttreatments, which was a key advantage for the fabrication of rapidly deployable autonomous robots.

Monolithic printed autonomous gripper

Building on the fabrication method as well as the actuator and valve designs discussed in the previous sections, we demonstrated a fabrication approach that is uniquely enabled by 3D printing. We designed a monolithic autonomous gripper with integrated control circuitry that can be 3D-printed on a desktop FFF printer in a one-shot workflow. The integrated fluidic control system allowed the gripper to be powered by a single constant pressure source and realized both gripping and releasing functions autonomously with fluidic sensors and feedback control circuits.

The printed autonomous gripper consisted primarily of two curved actuators and two control valves as demonstrated in the previous sections (Fig. 5). We also designed a contact switch and a gravity switch to control the gripping and releasing actions, respectively. Interconnecting tubing was designed on top of the entire structure to conduct airflow to the fluidic components (see fig. S5). The electronics-free operation procedure of the gripper included four states: (i) standby, (ii) gripping, (iii) holding, and (iv) releasing (Fig. 5B and movie S5). In the standby state, the gripper was connected to a 15-psi constant-pressure supply. Because the

pressure was applied to the control port of the output valve, the two bending actuators stayed in an unactuated state. In the gripping state, the gripper was pressed vertically on top of an object, closing the contact switch. The force applied on the contact switch caused air pressure to build and press the control port of the control valve. With the control valve pressed, the pressure was released from the control port of the output valve, enabling air to inflate the actuators and grip the object. In the holding state, the gripper was lifted to transport the object. In this state, if the contact switch lost contact with the object, then the gripper was still able to maintain a stable holding state because the closed output valve trapped high-pressure air in the gripper (movie S5). The gripped object was only released in the releasing state, in which the actuators were deflated when the whole gripper was turned to the horizontal direction. This state was initiated by the gravity switch that cut off the air supply to the entire circuit when closed, causing the air pressure throughout the circuit to release through the exhaust ports and opening the gripper. In our tests, the gripper was powered by a portable CO_2 canister. The operation did not rely on heavy air compressors or logical electric control circuits. All the states were performed by simple sensing and feedback controls.

The gripper was manufactured in a one-shot 3D printing workflow in 16 hours and 19 min (movie S6). Because each component was designed to be printed in layers consisting of Eulerian toolpaths, it was possible to achieve the same for the combined assembly, to realize an airtight design with low structural stiffness. As an example, fig. S6 and movie S7 show the toolpath on one of the representative layers that did not contain any free motions.

To autonomously respond when our gripper came into contact with an object, we required a printable contact switch (to be specific, a valve that closed in response to an applied force). We considered using a design that kinked a tube, similar to the control valve described above and a sensor used in a previous molded gripper (15). However, when printed out of TPU, the softest channels we could achieve required about 4 N of force to kink. To achieve a more sensitive response, we designed a different contact switch mechanism (Fig. 5C). The contact switch contained a contact pad to touch the objects, which was connected to the palm of the gripper by multiple soft suspension structures on both sides. As shown in the right-side sectional cut view of Fig. 5C and fig. S4, there was a convex exhaust port in a pyramid shape on the main block, with a vent hole at the center. On the back side of the contact pad, there was a cap in the same pyramid shape as the exhaust port. The gap between the exhaust port and the cap in the assembly was about 0.5 mm. Therefore, exhaust airflow was able to move through the vent port and the gap. When a contact force was applied on the contact pad, the pyramid cap was pressed on the exhaust port to close the gap and block the airflow. In this design, the suspension springs were used to maintain the contact pad in position while providing little resistance when the pad was displaced. As a result, the contact switch was highly sensitive, and it was triggered by the weight of a 14-g metal key in our test (to be specific, 0.14 N or 0.031 lbf; movie S8). One important point to note here is that once the switch was triggered, it was not the case that the gripper released the object if the switch was no longer pressed. The gripper's fluidic circuit stored the "closed" state in memory and released the object only if the gravity sensor was triggered. Thus, the gripper was taking the information from the contact switch and acting on it in a more complex way than simply closing when an object was detected and opening
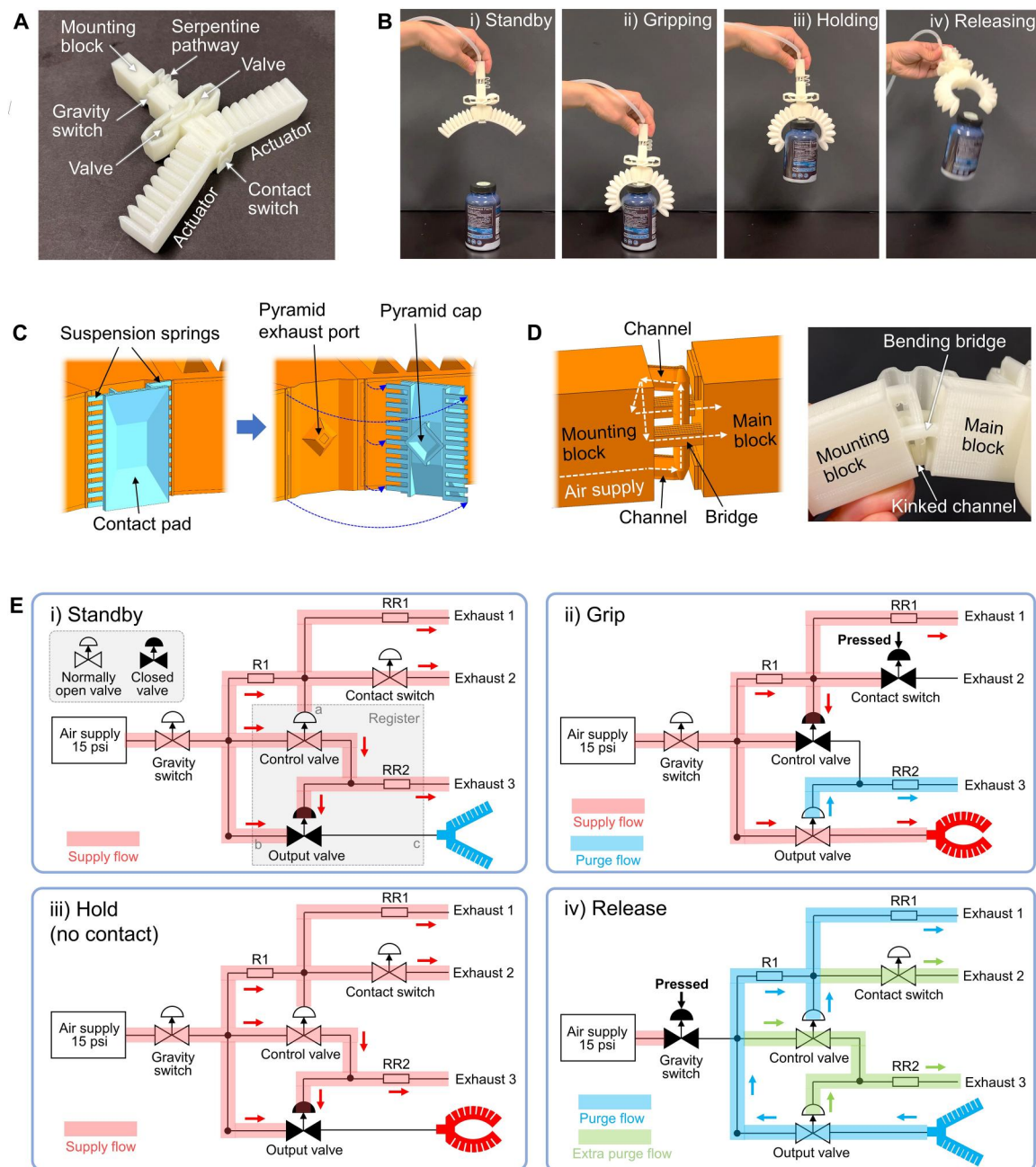
Fig. 5. Design, operation procedure, and working mechanism of the monolithic printed autonomous gripper. (**A**) Photograph of the monolithic printed autonomous gripper with key components labeled. (**B**) Images from the demonstration of the operation of the auto gripper (see movie S9). (**C**) CAD design of the contact switch in assembly view (left) and sectional cut view (right). (**D**) CAD design (left) and photograph (right) of gravity switch showing the mechanism for kinking the tubes to cut the supply of air. (**E**) Schematics of pneumatic control circuits in four different states corresponding to the states pictured in subfigure (B). (i) In the standby state, positive pressure applied to the control port of the output valve prevents air pressure from reaching the gripper. (ii) In the gripping state, the contact switch has been pressed, causing air pressure to build and press the control port of the control valve. With the control valve pressed, the pressure is released from the control port of the output valve, enabling air pressure to actuate the gripper. (iii) In the holding state, the closed output valve traps high-pressure air in the gripper, preventing it from opening even if the contact switch is no longer pressed. (iv) In the releasing state, the gravity switch cuts off the air supply to the entire circuit, causing the air pressure throughout the circuit to release through the exhaust ports and opening the gripper.

when it was not. In this sense, we see the information from the switch as a sensor input to the control algorithm of the gripper (encoded in the analog fluidic circuit).

The releasing function of our gripper was achieved with a gravity switch (Fig. 5D). The gravity switch was simply a valve controlling the main pressure supplied into the entire fluidic circuit. It consisted of two channels and two hollow bridges. The channels were on the top and bottom layers between the mounting block (grounded part of the gripper) and the main block (connected to the actuators) and could be kinked to shut off the airflow. The bridges were on the middle height of the structure, which was able to bend but could not be kinked. During operation, the supplied air coming from the mounting block flowed through the two channels in a series path, then turned back into the mounting block and passed through the two bridges to reach the main body (see left CAD design of Fig. 5D). As shown in the right photograph of Fig. 5D, when the gripper was turned to the side, the bridges bent as hinges between the mounting block and the main block, and the main block rotated downward by gravity to kink the lower channel. As a result, the main pressure supply was cut, and the object was released. We designed the bridges with thicker walls than the channels to avoid being kinked when pushing the gripper downward in the gripping state (movie S9).

Analogous to electrical circuits, we could model the flow of air through our fluidic control circuit with a lumped parameter model (fig. S7). Figure 5E shows four versions of this circuit annotated to represent the airflow and valve states during the four gripper operations described in detail below. The three resistors marked as R1, RR1, and RR2 represent the lumped fluid resistance of thin tubes connecting the corresponding components. The diameters of the tubes represented by RR1 and RR2 were thinner than that of R1 to achieve higher resistance. The mechanisms of all the states are explained below.

Standby

The system was connected to a 15-psi air supply, and both the gravity and contact switches were not pressed. There was a small airflow through resistor R1, and it vented through the open port of the contact switch (exhaust 2). In this case, the pressure did not build up at the control port of the control valve, so the valve remained in the unactuated open state. Airflow passed through the channel of the control valve to reach the control port of the output valve. Because of the resistance of RR2, the venting airflow was low, and pressure built up at the control port of the output valve. The actuated output valve prevented the air supply from reaching the actuators, so the actuators remained in the unactuated state.

Grip

The contact switch was pressed, and exhaust 2 was blocked. The airflow passed through R1 encountered high resistance when venting through RR1 and exhaust 1. Therefore, the pressure at the control port of the control valve increased to close the valve. At this time, the air inflated in the control chamber of the output valve fully purged through RR2 and exhaust 3. The output valve was open, and airflow inflated the actuators.

Hold

If the gripped object was sufficiently large and had a convex top surface (for example, as a tennis ball), after gripping, it still maintained contact with the contact switch. The flow logic in the holding state was the same as that in the gripping state, and the actuators were constantly connected to the air supply. However, if the

object was smaller and/or had a nonconvex top surface (for example, a cup), when it was lifted, then the contact switch had a chance to lose contact with the object. In this situation, as shown in diagram (iii), the output valve was closed, whereas the air inflated in the actuators was trapped. In this case, the gripper was still able to maintain a grip on the object.

Release

In the release state, when the gravity switch was activated, the main air supply was cut off. Initially, if an object was still in contact with the switch, then the control valve remained closed, and air in the actuators purged through exhaust 1. At the point when no object was touching the contact switch, the control valve opened, allowing the actuators to also purge through exhaust 2 and exhaust 3. Last, after a complete purging, the actuators were opened, and the gripper returned to standby mode for future operation cycles.

In this pneumatic control circuit, two valves were connected in series to control the actuators. Each of the normally open valves worked as an inverter, so the combination of two inverters in series was a forward amplifier (similar to a Darlington configuration in electronics) (65), which also had the function of a register, as shown in the shaded region in Fig. 5Ei. Besides power and exhaust ports, the register had three functional ports, marked as a, b, and c. If the contact switch was pressed, a positive pressure signal was applied to port a, then port b and port c were connected, and the pressure at port c was synchronized with that at port b. When port a was depressurized, port b and port c were isolated, and the pressure at port c was locked at the previously synchronized pressure. This logic could write and store pressure at port c. Because a constant power supply was required to maintain the states, it was a volatile memory. Therefore, the stored pressure could be erased by pressing the gravity switch to cut off the main pressure supply.

The three resistors placed in the circuit had critical roles. Resistor R1 was used to reduce the pressure of airflow from the supply, so the pressure at the control port of the control valve was kept at a low level when the contact switch was open. Resistor RR1 was used in the case of releasing an object that was always in good contact with the contact switch. In this case, the control valve was always closed, and exhaust 2 was also blocked. After cutting off the air supply, the trapped air was not able to purge through exhaust 2 or exhaust 3. Therefore, the extra exhaust port 1 was necessary for the releasing operation. However, it was also important that the resistance of RR1 was relatively high. This ensured that, when the contact switch was pressed, the pressure applied to the control port of the control valve would increase and not vent too easily through exhaust 1. Similarly, resistor RR2 had a high enough resistance to build up a high pressure at the control port of the output valve when the control valve was open and to purge the inflated air in the output valve when the control valve was closed.

DISCUSSION

In this work, we designed a monolithic autonomous gripper, which was fabricated in a one-shot (uninterrupted) 3D printing workflow and was ready to use immediately after printing. The gripper was designed to autonomously pick up and release objects with simple controls and could be a useful manipulation tool in various applications such as manufacturing and farming. In the fabrication process, there was no manual operation such as assembly or adjustment required, implying that the process and design are easily

reproducible using a similar desktop 3D printer. In our printed gripper, multiple functional components were designed "in silico" separately and combined in CAD into a single design to achieve complex tasks. With our predefined toolpath rules, all parts and the combined system were in the same printing standard to maintain the working performance and airtight quality.

The main function of our autonomous gripper was to use feedback from a contact switch to grip an object and hold it until another switch (a gravity switch) was activated. The contact switch on the gripper transferred the contact force to a pressure signal as an input to the logical circuit. On the output side, the bending actuators were inflated by high-pressure air as a response. The logic in this pneumatic circuit was an amplifier, in which the output was positively correlated to the input. To achieve this logic, a normally closed valve was required, which was equivalent to an N-channel MOS (NMOS) transistor in electric circuits. However, it was challenging to fabricate a normally closed pneumatic valve by monolithic 3D printing because the valve required a channel that was always in the kinked state, with built-in stress. Without manual post-operation, the printer was not able to apply force on the channel to kink. In contrast, the printing of normally open valves was less challenging. Therefore, our design comprised two normally open valves instead of a normally closed valve.

Beyond the gripper presented here, a similar approach could be applied to the design and fabrication of a range of pneumatic devices with embedded sensing and control circuits. To 3D-print monolithic devices, we devised a set of design rules that resulted in 3D-printed layers with Eulerian toolpaths. The restriction of Eulerian paths avoided instances of retraction and free motion of the print head because we found that the retraction of soft filament was not effective on desktop 3D printers and led to air leaks in the structure. Using Eulerian paths, the nozzle could print each layer in a single continuous path at a constant extrusion rate. As a result, the structures of all the vertical walls were unified to the same standard, including wall thickness, trace overlap, and printing speed. The vertical walls printed in this approach were thinner than the ones reported in the previous work while being airtight.

The design rules we have identified, however, do place constraints on the design space. To achieve Eulerian paths, there should be no isolated structures on any layers. Thus, for the case where separated structures were desired, we needed to add printed pathways to allow the nozzle to move between them. These pathways added undesired stiffness when there was relative movement between the components, which reduced the performance of some devices. To reduce the unwanted resistance, we designed these connecting pathways to have serpentine (Fig. 5A) or hollow suspension (Fig. 5C) shapes. When there was relative bending or translation between the two parts, the soft pathways connecting them could deform easily. In cases where large relative movement or continuous rotation was needed, one may need to consider alternative approaches.

To realize the functions of the autonomous gripper, we designed four different printed functional pneumatic devices: a bending actuator, a normally open valve, a contact switch, and a gravity switch, as well as some supporting structural frames and pneumatic interconnections. These individual components can be treated as "building blocks," which, when combined in an intelligent manner using CAD, resulted in the final design and functionality of the autonomous gripper. One can imagine following a similar approach to designing customized products with different capabilities by combining these "building blocks" in CAD. If the resulting design still follows the rules described here, then we expect the monolithic printing to be successful. For example, a complex gripper could be designed by combining more contact switches and actuators, which would be able to pick up multiple objects separately and transport them to the final destination together. Such a design could be used for farming in the harvesting of fruits with high efficiency.

In summary, we designed a monolithic printed autonomous gripper that was fabricated in a one-shot (uninterrupted) workflow. The gripper can be duplicated simply by desktop printers. The design rules presented in this work can be used to create air-tight high-performance autonomous pneumatic devices. With different combinations of the "building blocks," customized complex robots can be designed and manufactured in monolithic printing processes.

MATERIALS AND METHODS

Printing of pneumatic devices

We printed all the pneumatic devices in this work using a commercially available desktop 3D printer (Raise 3D E2, Raise 3D Technologies, Inc.) with some modifications. First, the user-interface computer in the printer was disconnected, and a laptop computer was connected to the motion control board in the printer by a USB cable. Printing monitoring software (Repetier-Server, Hot-World GmbH & Co. KG) running on the laptop computer was used to control all the printing tasks. Second, we added an extra cooling fan to the print head assembly to cool down the printed workpiece at a faster rate. The printing materials were experimental 80A TPU filaments provided by BASF Forward AM. The parameters used for printing are shown in table S1.

Generation of the Eulerian toolpaths

The generation of the Eulerian toolpaths was mainly performed by the slicer software (ideaMaker, Raise 3D Technologies, Inc.) using the following three design rules that were applied during the original CAD design process: First, we designed all vertical walls to have a thickness of 0.6 mm. Second, we connected independent components (which would require separate toolpath segments) with 0.6-mm-wide bridges. If relative movement was required between two components, then we reduced the stiffness of these bridges by giving them zigzag or serpentine shapes. Third, in the case of loop structures (which would create separate toolpaths), we added a 0.02-mm gap to one part of the loops. This caused the slicer to integrate the loop into the Eulerian toolpath. However, the small size of the gap caused the adjacent structures to fuse together when printed.

For parts designed following the three rules described above, we only had to adjust one parameter in the slicer software to ensure it generated Eulerian toolpaths: the linewidth/nozzle size, which was set to 0.3 mm. The slicer also outlines the exterior of each layer before filling any internal volume. We found that this parameter (the number of outline layers) did not affect the Eulerian path and could be set to any value. In our experiments, we set this parameter to two, which we found to work best for the solid structures at the top and bottom of the parts (to be specific, any horizontal walls at the top and bottom of the parts).

Characterization of printed bending actuators

The air supply was regulated by proportional pressure-regulating valves (VPPE-3-3-1, Festo Corporation). We made a customized digital controller to control four regulating valves. The controller was connected to a computer with a serial interface. Each regulator was able to output pressure in the range of 0.4 to 25.5 psi with a resolution of 0.1 psi. The regulated pressure was supplied to the bending actuators for underwater leakage, blocked force, and free strain tests. In the blocked force characterization, an S-type load cell (DY106-3 kg, Shanghai Qiyi Co., Ltd.) was used to measure the force. The analog feedback value from the load cell was sampled by an AD converter (HX-711, DIYmall) with an Arduino controller, which was connected to the computer with serial communication. A MATLAB program was used to control the output pressure of the regulating valve and record the force value from the AD converter.

Characterization of printed valves

Two regulating valves were used to supply pressures to the control port and one of the two channel ports of the printed valve, respectively. The flow rate through the channel was measured at the other channel port of the valve, which was connected to the common port of a solenoid 3/2 valve. The two selection ports of the 3/2 valves were connected to a high-range flow meter (FS1023-1001-DG, Renesas Electronics Corporation) and a low-range flow meter (G6691A ADM Flow Meter, Agilent Technologies), respectively. The high-range flow meter has a range of 10 to 10,000 SCCM with an accuracy of 20 SCCM, and the low-range flow meter has a range of 0 to 750 SCCM with an accuracy of 0.2 SCCM. During each flow characterization of the printed valve, constant pressure was supplied to the channel, and the pressure supplied to the control port was increased gradually until the valve was fully closed. In the beginning, the solenoid 3/2 valve was used to direct the airflow to the high-range flow meter. When the airflow dropped to below 600 SCCM, the 3/2 valve redirected the airflow to the low-range flow meter to measure precise values. In the durability tests of the printed valve, only the high-range flow meter was used to measure the airflow in each open and closed state.

Electronics-free operation of the autonomous gripper

In the demonstration of the autonomous gripper, we used 16-g compressed CO_2 canisters (threaded CO_2 cartridge refills, Cycling Deal USA Inc.) to supply a constant pressure. Each canister contained 14.5 ml of liquid CO_2, and the maximum output pressure was 5.9 MPa (860 psi). A mechanical regulator (mini CO_2 gas regulator soda pressure gauge, AUNMAS) was used to regulate the pressure to about 103 kPa (15 psi). Each canister was able to power the gripper for about 50 s.

Supplementary Materials

This PDF file includes:
Figs S1 to S7
Tables S1 to S3
References (66, 67)

Other Supplementary Material for this manuscript includes the following:
Movies S1 to S9
Data file S1

REFERENCES AND NOTES

1. T. J. Wallin, J. Pikul, R. F. Shepherd, 3D printing of soft robotic systems. *Nat. Rev. Mater.* **3**, 84–100 (2018).
2. S. Kim, C. Laschi, B. Trimmer, Soft robotics: A bioinspired evolution in robotics. *Trends Biotechnol.* **31**, 287–294 (2013).
3. D. Rus, M. T. Tolley, Design, fabrication and control of soft robots. *Nature* **521**, 467–475 (2015).
4. R. F. Shepherd, F. Ilievski, W. Choi, S. A. Morin, A. A. Stokes, A. D. Mazzeo, X. Chen, M. Wang, G. M. Whitesides, Multigait soft robot. *Proc. Natl. Acad. Sci. U.S.A.* **108**, 20400–20403 (2011).
5. Y. Tang, Q. Zhang, G. Lin, J. Yin, Switchable adhesion actuator for amphibious climbing soft robot. *Soft Robot.* **5**, 592–600 (2018).
6. C. Laschi, B. Mazzolai, V. Mattoli, M. Cianchetti, P. Dario, Design of a biomimetic robotic octopus arm. *Bioinspir. Biomim.* **4**, 015006 (2009).
7. C. D. Onal, D. Rus, Autonomous undulatory serpentine locomotion utilizing body dynamics of a fluidic soft robot. *Bioinspir. Biomim.* **8**, 026003 (2013).
8. M. T. Tolley, R. F. Shepherd, B. Mosadegh, K. C. Galloway, M. Wehner, M. Karpelson, R. J. Wood, G. M. Whitesides, A resilient, untethered soft robot. *Soft Robot.* **1**, 213–223 (2014).
9. D. Drotman, S. Jadhav, D. Sharp, C. Chan, M. T. Tolley, Electronics-free pneumatic circuits for controlling soft-legged robots. *Sci. Robot.* **6**, 10.1126/scirobotics.aay26, (2021).
10. F. Ilievski, A. D. Mazzeo, R. F. Shepherd, X. Chen, G. M. Whitesides, Soft robotics for chemists. *Angew. Chem. Int. Ed. Engl.* **50**, 1890–1895 (2011).
11. R. Adam Bilodeau, E. L. White, R. K. Kramer, Monolithic fabrication of sensors and actuators in a soft robotic gripper, in *2015 IEEE/RSJ International Conference on Intelligent Robots and Systems* (IEEE, 2015), pp. 2324–2329.
12. Y. Wei, Y. Chen, T. Ren, Q. Chen, C. Yan, Y. Yang, Y. Li, A novel, variable stiffness robotic gripper based on integrated soft actuating and particle jamming. *Soft Robot.* **3**, 134–143 (2016).
13. J. Zhou, S. Chen, Z. Wang, A soft-robotic gripper with enhanced object adaptation and grasping reliability. *IEEE Robot. Autom. Lett.* **2**, 2287–2293 (2017).
14. Y. Hao, Z. Gong, Z. Xie, S. Guan, X. Yang, Z. Ren, T. Wang, L. Wen, Universal soft pneumatic robotic gripper with variable effective length, in *Chinese Control Conference (CCC)* (IEEE, 2016), pp. 6109–6114.
15. P. Rothemund, A. Ainla, L. Belding, D. J. Preston, S. Kurihara, Z. Suo, G. M. Whitesides, A soft, bistable valve for autonomous control of soft actuators. *Sci. Robot.* **3**, eaar7986 (2018).
16. D. J. Preston, P. Rothemund, H. J. Jiang, M. P. Nemitz, J. Rawson, Z. Suo, G. M. Whitesides, Digital logic for soft devices. *Proc. Natl. Acad. Sci. U.S.A.* **116**, 7750–7759 (2019).
17. R. K. Katzschmann, A. D. Marchese, D. Rus, Hydraulic autonomous soft robotic fish for 3D swimming. *Springer Tracts Adv. Robot.* **109**, 405–420 (2016).
18. A. Joshi, A. Kulkarni, Y. Tadesse, FludoJelly: Experimental study on jellyfish-like soft robot enabled by soft pneumatic composite (SPC). *Robotics* **8**, 56 (2019).
19. C. A. Aubin, S. Choudhury, R. Jerch, L. A. Archer, J. H. Pikul, R. F. Shepherd, Electrolytic vascular systems for energy-dense robots. *Nature* **571**, 51–57 (2019).
20. H. Zhao, Y. Li, A. Elsamadisi, R. Shepherd, Scalable manufacturing of high force wearable soft actuators. *Extreme Mech. Lett.* **3**, 89–104 (2015).
21. P. Polygerinos, S. Lyne, Z. Wang, L. F. Nicolini, B. Mosadegh, G. M. Whitesides, C. J. Walsh, *IEEE International Conference on Intelligent Robots and Systems* 2013), 1512–1517.
22. P. Polygerinos, Z. Wang, K. C. Galloway, R. J. Wood, C. J. Walsh, Soft robotic glove for combined assistance and at-home rehabilitation. *Rob. Auton. Syst.* **73**, 135–143 (2015).
23. C. M. Schumacher, M. Loepfe, R. Fuhrer, R. N. Grass, W. J. Stark, 3D printed lost-wax casted soft silicone monoblocks enable heart-inspired pumping by internal combustion. *RSC Adv.* **4**, 16039–16042 (2014).
24. W. K. Lee, D. J. Preston, M. P. Nemitz, A. Nagarkar, A. K. MacKeith, B. Gorissen, N. Vasios, V. Sanchez, K. Bertoldi, L. Mahadevan, G. M. Whitesides, A buckling-sheet ring oscillator for electronics-free, multimodal locomotion. *Sci. Robot.* **7**, eabg5812 (2022).
25. S. Wang, L. He, P. Maiolino, A modular approach to design multi-channel bistable valves for integrated pneumatically-driven soft robots via 3D-printing. *IEEE Robot. Autom. Lett.* **7**, 3412–3418 (2022).
26. H. Lipson, J. B. Pollack, Automatic design and manufacture of robotic lifeforms. *Nature* **406**, 974–978 (2000).
27. M. K. Hod Lipson, *Fabricated the New World of 3D Printing* (John Wiley&Sons Inc, ed. 1, 2013), pp. 1–5.
28. O. D. Yirmibesoglu, J. Morrow, S. Walker, W. Gosrich, R. Canizares, H. Kim, U. Daalkhaijav, C. Fleming, C. Branyan, Y. Menguc, Direct 3D printing of silicone elastomer soft robots and their performance comparison with molded counterparts, in *2018 IEEE International Conference on Soft Robotics (RoboSoft)* (IEEE, 2018), pp. 295–302.

29. J. D. Carrico, K. J. Kim, K. K. Leang, 3D-printed ionic polymer-metal composite soft crawling robot, in *IEEE International Conference on Robotics and Automation (ICRA)* (IEEE, 2017), pp. 4313–4320.

30. N. W. Bartlett, M. T. Tolley, J. T. B. Overvelde, J. C. Weaver, B. Mosadegh, K. Bertoldi, G. M. Whitesides, R. J. Wood, A 3D-printed, functionally graded soft robot powered by combustion. *Science* **349**, 161–165 (2015).

31. J. D. Hubbard, R. Acevedo, K. M. Edwards, A. T. Alsharhan, Z. Wen, J. Landry, K. Wang, S. Schaffer, R. D. Sochol, Fully 3D-printed soft robots with integrated fluidic circuitry. *Sci. Adv.* **7**, eabe5257 (2021).

32. Y. Zhai, T. N. Ng, Self-sustained robots based on functionally graded elastomeric actuators carrying up to 22 times their body weight. *Advanced Intelligent Systems* **5**, 2100085 (2023).

33. A. Zolfagharian, M. A. P. Mahmud, S. Gharaie, M. Bodaghi, A. Z. Kouzani, A. Kaynak, 3D/4D-printed bending-type soft pneumatic actuators: Fabrication, modelling, and control. *Virtual Phys. Prototyp.* **15**, 373–402 (2020).

34. M. Wehner, R. L. Truby, D. J. Fitzgerald, B. Mosadegh, G. M. Whitesides, J. A. Lewis, R. J. Wood, An integrated design and fabrication strategy for entirely soft, autonomous robots. *Nature* **536**, 451–455 (2016).

35. D. Drotman, S. Jadhav, M. Karimi, P. Dezonia, M. T. Tolley, 3D printed soft actuators for a legged robot capable of navigating unstructured terrain, in *2017 IEEE International Conference on Robotics and Automation (ICRA)* (IEEE, 2017), pp. 5532–5538.

36. G. D. Howard, J. Brett, J. O'Connor, J. Letchford, G. W. Delaney, One-shot 3D-printed multimaterial soft robotic jamming grippers. *Soft Robot.* **9**, 497–508 (2022).

37. Z. Wang, M. Zhu, S. Kawamura, S. Hirai, Comparison of different soft grippers for lunch box packaging. *Robot. Biomim.* **4**, 10 (2017).

38. T. Umedachi, V. Vikas, B. A. Trimmer, Softworms: The design and control of non-pneumatic, 3D-printed, deformable robots. *Bioinspir. Biomim.* **11**, 025001 (2016).

39. Z. Wang, S. Hirai, A 3D printed soft gripper integrated with curvature sensor for studying soft grasping, in *2016 IEEE/SICE International Symposium on System Integration (SII)* (IEEE, 2017), pp. 629–633.

40. S. M. Oskui, G. Diamante, C. Liao, W. Shi, J. Gan, D. Schlenk, W. H. Grover, Assessing and reducing the toxicity of 3D-printed parts. *Environ. Sci. Technol. Lett.* **3**, 1–6 (2016).

41. M. Carve, D. Wlodkowic, 3D-printed chips: Compatibility of additive manufacturing photopolymeric substrata with biological applications. *Micromachines (Basel)* **9**, 91 (2018).

42. N. P. MacDonald, F. Zhu, C. J. Hall, J. Reboud, P. S. Crosier, E. E. Patton, D. Wlodkowic, J. M. Cooper, Assessment of biocompatibility of 3D printed photopolymers using zebrafish embryo toxicity assays. *Lab. Chip* **16**, 291–297 (2016).

43. M. S. Xavier, C. D. Tawk, Y. K. Yong, A. J. Fleming, 3D-printed omnidirectional soft pneumatic actuators: Design, modeling and characterization. *Sensors Actuators A Phys.* **332**, 113199 (2021).

44. B. N. Peele, T. J. Wallin, H. Zhao, R. F. Shepherd, 3D printing antagonistic systems of artificial muscle using projection stereolithography. *Bioinspir. Biomim.* **10**, 055003 (2015).

45. D. K. Patel, A. H. Sakhaei, M. Layani, B. Zhang, Q. Ge, S. Magdassi, Highly stretchable and UV curable elastomers for digital light processing based 3D printing. *Adv. Mater.* **29**, 1606000 (2017).

46. Formlabs, "Material Data Sheet: Elastic 50A" (2019); https://formlabs-media.formlabs.com/datasheets/2001420-TDS-ENUS-0.pdf.

47. BASF, "Thermoplastic Polyurethane Elastomers (TPU) Elastollan - Product Range" (2016); www.basf.com/kr/documents/ko/product/Thermoplastic%20Polyurethane_Elastollan_Product%20Range.pdf.

48. Smooth-On, "Dragon Skin Series Technical Bulletin"; www.smooth-on.com/tb/files/DRAGON_SKIN_SERIES_TB.pdf.

49. H. K. Yap, H. Y. Ng, C. H. Yeow, High-force soft printable pneumatics for soft robotic applications. *Soft Robot.* **3**, 144–158 (2016).

50. B. A. W. Keong, R. Y. C. Hua, A novel fold-based design approach toward printable soft robotics using flexible 3D printing materials. *Adv. Mater. Technol.* **3**, 1700172 (2018).

51. D. Gonzalez, J. Garcia, R. M. Voyles, R. A. Nawrocki, B. Newell, Characterization of 3D printed pneumatic soft actuator. *Sensors Actuators A Phys.* **334**, 113337 (2022).

52. C. J. Hohimer, G. Petrossian, A. Ameli, C. Mo, P. Pötschke, 3D printed conductive thermoplastic polyurethane/carbon nanotube composites for capacitive and piezoresistive sensing in soft pneumatic actuators. *Addit. Manuf.* **34**, 101281 (2020).

53. R. Mutlu, C. Tawk, G. Alici, E. Sariyildiz, A 3D printed monolithic soft gripper with adjustable stiffness, in *IECON 2017-43rd Annual Conference of the IEEE Industrial Electronics Society* (IEEE, 2017), pp. 6235–6240.

54. A. Heiden, D. Preninger, L. Lehner, M. Baumgartner, M. Drack, E. Woritzka, D. Schiller, R. Gerstmayr, F. Hartmann, M. Kaltenbrunner, 3D printing of resilient biogels for omnidirectional and exteroceptive soft actuators. *Sci. Robot.* **7**, eabk2119 (2022).

55. A. Georgopoulou, L. M. Eckey, S. Mondal, F. Clemens, Case study of a rapid prototyping method for optimizing soft gripper structures with integrated piezoresistive sensors, in *2022 IEEE 5th International Conference on Soft Robotics (RoboSoft)* (IEEE, 2022), pp. 539–544.

56. A. Georgopoulou, L. Egloff, B. Vanderborght, F. Clemens, A sensorized soft pneumatic actuator fabricated with extrusion-based additive manufacturing. *Actuators* **10**, 102 (2021).

57. L. Wilhelm, Design of 3D-printed soft pneunet actuator for robotic fruit harvesting, thesis, Oregon State University (2022).

58. S. Conrad, T. Speck, F. J. Tauber, Tool changing 3D printer for rapid prototyping of advanced soft robotic elements. *Bioinspir. Biomim.* **16**, 055010 (2021).

59. T. Hainsworth, L. Smith, S. Alexander, R. MacCurdy, A fabrication free, 3D printed, multi-material, self-sensing soft actuator. *IEEE Robot. Autom. Lett.* **5**, 4118–4125 (2020).

60. L. Euler, Solutio problematis ad geometriam situs pertinentis. *Comment. Acad. Sci. Petropolitanae* **7**, 128–140 (1741).

61. C. Tawk, Y. Gao, R. Mutlu, G. Alici, Fully 3D printed monolithic soft gripper with high conformal grasping capability, in *2019 IEEE/ASME International Conference on Advanced Intelligent Mechatronics (AIM)* (IEEE, 2019), pp. 1139–1144.

62. B. Mosadegh, P. Polygerinos, C. Keplinger, S. Wennstedt, R. F. Shepherd, U. Gupta, J. Shim, K. Bertoldi, C. J. Walsh, G. M. Whitesides, Pneumatic networks for soft robotics that actuate rapidly. *Adv. Funct. Mater.* **24**, 2163–2170 (2014).

63. J. A. Tracz, L. Wille, D. Pathiraja, S. V. Kendre, R. Pfisterer, E. Turett, C. K. Abrahamsson, S. E. Root, W. K. Lee, D. J. Preston, H. J. Jiang, G. M. Whitesides, M. P. Nemitz, Tube-balloon logic for the exploration of fluidic control elements. *IEEE Robot. Autom. Lett.* **7**, 5483–5488 (2022).

64. J. E. Akin, in *Finite Element Analysis Concepts* (World Scientific Publishing Company, 2010), p. 205.

65. V. A. K. Temple, MOS-controlled thyristors—A new class of power devices. *IEEE Trans. Electron. Devices* **33**, 1609–1618 (1986).

66. P. Glick, S. A. Suresh, D. Ruffatto, M. Cutkosky, M. T. Tolley, A. Parness, A soft robotic gripper with Gecko-inspired adhesive. *IEEE Robot. Autom. Lett.* **3**, 903–910 (2018).

67. B. Shih, C. Christianson, K. Gillespie, S. Lee, J. Mayeda, Z. Huo, M. T. Tolley, Design considerations for 3D printed, soft, multimaterial resistive sensors for soft robotics. *Front. Robot. AI.* **6**, 30 (2019).

Acknowledgments

Science Robotics

Desktop fabrication of monolithic soft robotic devices with embedded fluidic control circuits

Yichen Zhai, Albert De Boer, Jiayao Yan, Benjamin Shih, Martin Faber, Joshua Speros, Rohini Gupta, and Michael T. Tolley

Sci. Robot., **8** (79), eadg3792.
DOI: 10.1126/scirobotics.adg3792

View the article online
https://www.science.org/doi/10.1126/scirobotics.adg3792
Permissions
https://www.science.org/help/reprints-and-permissions

Downloaded from https://www.science.org on June 21, 2023

Use of this article is subject to the Terms of service

Science Robotics (ISSN) is published by the American Association for the Advancement of Science. 1200 New York Avenue NW, Washington, DC 20005. The title *Science Robotics* is a registered trademark of AAAS.

Copyright © 2023 The Authors, some rights reserved; exclusive licensee American Association for the Advancement of Science. No claim to original U.S. Government Works